Journal of Alloys and Compounds 843 (2020) 155927

Contents lists available at ScienceDirect

Journal of Alloys and Compounds

journal homepage: http://www.elsevier.com/locate/jalcom

Phase integrity of zinc oxide doped zirconia under low compacting pressure

Shramana Mishra [a], Kundan Kumar [b], Atanu Patra [a], Anirban Chowdhury [b, **], Anushree Roy [a, *]

[a] Department of Physics, Indian Institute of Technology Kharagpur, West Bengal, 721302, India
[b] Metallurgical and Materials Engineering, Indian Institute of Technology, Patna, Bihar, 801106, India

ARTICLE INFO

Article history:
Received 24 March 2020
Accepted 3 June 2020
Available online 11 June 2020

ABSTRACT

The phase stability of zirconia (ZrO_2) under external perturbation draws the attention of researchers, as it governs the practical use of this material in technological applications. In this article, the phase transition in zinc oxide (ZnO) doped ZrO_2 is addressed by exploiting complementary methodologies, X-ray diffraction, and Raman spectroscopic measurements. We have observed a pressure-induced partial phase transformation in the doped ZrO_2 system for a compacting pressure of less than 1 GPa. It is noteworthy that the level of compacting pressure used in this study is much lower than the range of pressure, reported in the literature, for observing phase transition in pure and doped ZrO_2 using other high-pressure experiments. To understand the underlying dynamics of low pressure-induced phase transformation, we carried out density functional theory calculations for the doped supercell. We have discussed the local bonding environment around the dopant metal ion (Zn^{2+} in the present case), which, we believe, leads to the phase evolution in a real system.

1. Introduction

Zirconia (ZrO_2) is one of the many ceramic materials, which finds a broad range of technological applications [1–4]. The excellent mechanical properties, like, high-temperature strength [3], fracture toughness [2], etc. make it an important candidate for manufacturing various devices, especially in the medical field. These attractive characteristics are, however, largely associated with the tetragonal (*T*-) and cubic (*C*-) phases of ZrO_2. The monoclinic (*M*-) phase of ZrO_2 is thermodynamically most stable at room temperature and ambient pressure. With an increase in temperature, it undergoes the phase transition by following: $M \rightarrow T \rightarrow C \rightarrow$ melt.

Attempts have been made to stabilize the *T*- and the *C*- structure at ambient temperature by appropriate chemical substitution in the ZrO_2 matrix. This is accomplished by the replacement of some of the tetravalent Zr^{4+} ions (ionic radius of ~84 pm [5]) with slightly larger ions, like, trivalent yttrium ions (Y^{3+}: ionic radius of ~102 pm [5]) or divalent calcium ions (Ca^{2+}: ionic radius of ~100 pm [5]) [6,7]. In a recent study, the stabilizations of *T*- and *C*- phases at room temperature are achieved by doping Sc_2O_3 in ZrO_2 [8]. Here, the ionic radius of the scandium ion (Sc^{3+}: ionic radius of ~87 pm [5]) is comparable with that of the Zr^{4+} ion. In the process of aliovalent substitutions, oxygen vacancies are generated to maintain the charge neutrality. The presence of these vacancies leads to internal stress, which, in turn, causes a local distortion in the lattice. The dynamics of phase transformation of doped ZrO_2 is complex and strongly depends on external conditions, like the annealing temperature, applied pressure, etc. [6–14].

Reports in the literature on the pressure-induced phase transformations in both undoped and doped ZrO_2 systems are quite diverse with a variety of observations and explanations [9,10,15–21]. The most commonly observed pressure-induced phase transition in the case of undoped zirconia is from $M \rightarrow T$-phase and from $T \rightarrow C$-phase [15–20]. Perry et al. [19] had observed a transition from an *M*-phase to a distorted *T*-phase at a pressure of about 4.1 GPa. Also, in the high applied pressure (~31 GPa) regime, an evolution towards a distorted cubic structure has been experimentally observed [15]. Density functional theory (DFT) studies on the undoped system revealed that the pressure-induced phase

* Corresponding author.
** Corresponding author.
E-mail addresses: anirban.chowdhury@gmail.com (A. Chowdhury), anushree@phy.iitkgp.ac.in (A. Roy).

https://doi.org/10.1016/j.jallcom.2020.155927
0925-8388/

transition proceeds from an *M*-phase to a *T*-phase via a structurally unstable orthorhombic phase [20]. Further calculations show that for the *T*-phase, externally applied pressure removes tetragonal distortions, and the structure transforms into a *C*- phase [17].

For doped ZrO_2, however, the mechanism of phase transformation is very different from that of the undoped compound. Though in the literature, a large number of articles discussed the phenomenon using a variety of dopants like Y_2O_3, CaO, Sc_2O_3, etc. [6–10], the contradicting reports hinder us to conclusively comment on the origin of the phase transition in this system. Phase transformation in the doped system not only depends on the dopant type but also on the relative concentration of the dopant. While the phase transition could not be observed in phase stabilized Y_2O_3 (5.3 wt %) doped ZrO_2 under different compressive stress (0–0.9 GPa) [10], the low pressure-induced (0.1 GPa) martensitic phase transformation from the metastable *T*→ *M*-phase has been reported by Majumder and Chatterjee [21] in compacted Y_2O_3 (3 mol %) doped ZrO_2. In this case, the phase transformation is mediated by the segregation of the dopants to surface and grain boundaries. On the other hand, for 3 wt % Y_2O_3-ZrO_2 system [a phase mixture of *M*- (~80%) and *T*- (~20%) ZrO_2], *M*→*T*-ZrO_2 transformation was observed on the application of pressure of 4.2 GPa; the final *T*-phase content was noted to be ~85% [9].

In this article, we probe the possibility of utilizing a multifunctional oxide, like ZnO for stabilizing the ZrO_2 matrix to a desired structural phase. As Zn^{+2} is a divalent ion, more oxygen vacancies (1 vacancy per dopant) are expected to be bound within the local structure of the doped compound than what we find in the cases of Y_2O_3 and Sc_2O_3 doping (1 vacancy per 2 dopants). It is also non-trivial to compare the process of phase transition as a result of doping of two different divalent ions. The ionic radius of Zn^{2+} (60 pm [5]) is much less than that of other divalent ions like Ca^{2+}. Hence, the lattice distortion, for compensating the volume reduction due to oxygen vacancies, is expected to be different in the case of CaO or ZnO doping, which can affect the phase stabilization of the system. For proper utilization of these materials in devices (in the form of bars, rods, etc.), the fabrication procedures require compacting pressure on the powder samples. Thus, it is important to investigate the underlying physics governing the phase stability of doped ZrO_2 under compaction for the efficient utilization of the material.

We have investigated the effect of compacting pressure on the phase transformation of the ZnO doped ZrO_2 of a mixed *C/T* phase, using X-ray diffraction (XRD) and Raman spectroscopic measurements. Our experimental observations suggest the formation of pressure-induced *M*-phase and distorted *T*-phase in the host matrix. Raman spectroscopy is a powerful tool to detect the changes in the atomic bonding of a system under external perturbation [6,8–11,15,19]. It is particularly sensitive to the polarizability of the oxygen ions. As the oxygen is expected to play a crucial role in phase transformations in ZrO_2, Raman spectroscopy can serve as a useful tool for studying the stability of the compound. In our study, while XRD measurements probe the overall structural phase in the system, Raman scattering yields the information of local structural disorder. Thus, these two complementary techniques render integral information of the structural stability of the compound. Furthermore, we have carried out DFT calculations to investigate the chemical bonding mechanism in ZnO doped ZrO_2, and the possible underlying dynamics of the experimentally observed phase transformation. There are few articles in the literature in which the formation and applications of *T*-phase stabilized by ZnO doped ZrO_2 are reported [11–13]. To the best of our knowledge, the effect of external compaction pressure on this doped compound is still missing in the literature. Noteworthy is the fact that the phase transformation, which we will discuss in this article, is irreversible in nature and has been observed at low pressure (<1 GPa). The specific role of mechanical stress to a phase transition during pelletization (compaction) may be different from the same reported using other high-pressure laboratory-based experiments (say, in the case of hydrostatic pressure-induced phase transition in doped and undoped ZrO_2 using a diamond anvil cell [9,10,15,17]). However, it is to be noted that the range of pressure used in this study is much lower than the pressure used in the literature to investigate the phase stability of various doped ZrO_2 compounds. The applied stress is very close to the nominal mechanical stress generally applied during normal processing operations (e.g., shaping, pressing of a green body). Our results indicate that the phase stability issues of the present system can influence these normal processing operations.

2. Experimental and simulation methodologies

8 mol.% ZnO doped ZrO_2 powder sample was synthesized using a co-precipitation method. The dried precipitates were calcined at 500 °C in the air for 2 h. We refer to this as-prepared powder as Sample A. For pressure dependent studies, the powder samples were pelletized at room temperature by pressing the powder between steel dies of diameter 10 mm. The applied pressure was in the range of 0.05 GPa–0.95 GPa. We refer to the compacted samples, under 0.05, 0.15, 0.25, 0.35, 0.45, 0.55, 0.65, 0.75, 0.85 and 0.95 GPa applied pressures, as Sample B–Sample K, respectively. The detail of the sample preparation procedure is available elsewhere [22].

The XRD measurements were carried out in θ–2θ geometry using Cu Kα radiation (λ = 1.5406 Å, Rigaku TTRX-III, Japan). The diffraction angle (2θ) was selected from 20° to 80° with a step size of 0.02° and a scan rate of 0.2°/min. The refinement of the XRD data was carried out using FULLPROF [23], a free software available online. The background was obtained using linear interpolation between 50 selected points. A Cauchy (Lorentzian) function was used to describe the peak shape. Various parameters, like the profile parameters, the scale factor, and the lattice parameters of different phases, were refined. For the refinement, the initial structural starting parameters for different phases were chosen from the corresponding JCPDS files.

Micro-Raman spectra were recorded at room temperature using a 532 nm excitation wavelength of a diode laser. The spectrometer was equipped with an optical microscope (model BX41, Make Olympus, Japan), a single monochromator (model IHR550, Make Horiba, France), and a Peltier cooled CCD (1024 × 256 pixels, model Synapse, Make Horiba, France) detector. For wavelength-dependent measurements, Raman spectra were recorded using several excitation wavelengths between 457.9 nm and 647.1 nm from Ar^+–Kr^+ laser (model Innova 70C, Coherent, USA). The measurements were carried out in back-scattering geometry using a triple monochromator (model T64000, Make JY, Horiba, France). In addition, Raman spectra of Sample K were recorded using 632 nm and 785 nm wavelengths of diode lasers and a single monochromator spectrometer (HR-800, Make JY, Horiba, France).

Furthermore, we carried out the first-principles calculations to estimate the Zr–O bond lengths in undoped and ZnO doped ZrO_2 systems using all-electron-full potential Wien2K code [24]. The simulations are carried out in the athermal limit, i.e, $T = 0$ K. For the optimization of the structures, we considered generalized gradient approximation (GGA) functional as mentioned in Ref. [25]. The spherical harmonic function inside the muffin-tin spheres was limited by $l_{max} = 12$, where the muffin-tin radii for Zr, O and Zn were fixed at 2.0, 1.6, and 1.95 a.u (atomic units), respectively. In interstitial regions, the charge density and potential were defined through G_{max} at 12 $Bohr^{-1}$. The R_{min}^{MT} K_{max} was fixed to 8 for all

calculations. The *k*-mesh for the calculation was 4 × 4 × 3. The force on each atom was relaxed by less than 0.5 mRyd/a.u.

3. Results

3.1. X-ray diffraction

The XRD patterns of as-prepared powder of ZnO doped ZrO_2 (Sample A) and samples compacted at different pressures (Sample B–Sample K) are shown in Fig. 1. All XRD patterns were analyzed using Rietveld refinement. The refined XRD patterns for few characteristic samples are shown in Fig. 2 [Sample A (as-prepared powder), Sample G (compacted at 0.55 GPa), and Sample K (compacted at 0.95 GPa)].

The XRD patterns of *C*-phase (JCPDS file no.49–1642) and *T*-phase (JCPDS file no. 50–1089) of ZrO_2 are very similar. The earlier report in the literature [22] suggests that in ZnO doped ZrO_2 both these phases are equiproportional. In the present analysis too, the best refinement of the data points could be obtained by taking into account a mixed contribution of *C*- and *T*-phase (with space group $Fm\bar{3}m$, and $P4_2/nmc$, respectively) (see Fig. 2(a) and Fig. S1 in the Supplementary Section for details). Similarly, the XRD patterns for Sample B and Sample C were best fitted with a mixed contribution of *C*- and *T*-phases. In Fig. 2, *C*- and *T*-ZrO_2 phases are indexed by green and orange bars, respectively. From the refinement of the pattern of Sample A, the lattice constants for the *T*-phase are found to be $a_T = 3.610$ Å and $c_T = 5.171$ Å. For the *C*-phase, the lattice constant a_C is estimated to be 5.094 Å. These values compare well with those published in the open literature [26,27]. For the Sample K (i.e., the sample compressed at the highest pressure), new features in the pattern could be clearly observed at both low and high diffraction angles (at ~28.4° and ~31.4°, respectively) with respect to the main peak (see the arrows for Sample K in Figs. 1 and 2). Hence, it was necessary to include the contribution of an additional phase (along with *T*- and *C*- phase) for the refinement. For *M*-ZrO_2, the $(\bar{1}11)$ and (111) diffraction peaks appear at ~ 28.2° and ~31.4°, respectively (with reference to the JCPDS file no. 37–1484). First, the pattern was fitted with *T*-, *C*- and *M*-phase, and the value of R_{wp} (weight profile R value) for the best fit was 15.7% (with $\chi^2 = 2.97$). The difference pattern showed a significant residual count at ~31.4°. For nanocrystalline undoped *T*- ZrO_2 pelletized at a pressure of 1.0 and 3.4 GPa, a peak appears at 31.4°, which has been attributed in the literature as the *T′*- phase (indexed with the JCPDS 13–4748) [17]. It can be considered as a new tetragonal modification of the *T*-phase, induced purely by the applied pressure. Thus, the diffraction pattern of the Sample K was refined with four phases, *T*-, *C*-, *M*- and *T′*- phase and the value of R_{wp} for the best fit was reduced to 14% (with $\chi^2 = 2.65$) (Refer to Fig. S2 of the Supplementary Section). In Fig. 2, the Bragg peaks of *M*- and *T′*- phase are indexed by purple and cyan bars, respectively. Similarly, the XRD patterns of Sample D–Sample J could be better refined by including the above four phases in our analysis. The refined pattern of the Sample G is also shown in Fig. 2. Table 1 lists the *T*-, *C*-, *M*- and *T′*- phase fractions in all samples under study, as obtained from the Rietveld refinement of the XRD data. From Table 1, it can be observed that up to a compacting pressure of 0.85 GPa (Sample J), the contributions of both *M*- and *T′*- phases in the diffraction patterns are either nil or significantly less than the same of *T*- and *C*- phases. In fact, for Sample D-Sample H, the minor phase (i.e., *M*- and *T′*-phases) fractions are negligible (~1%). The significant presence of *M*-phase in all samples as observed in our Raman measurements (shown later) and the possibility of the existence of *T′*-phase in the doped structure as obtained from DFT calculations (discussed later) compelled us to consider the contributions of these minor phases in the refinement of the XRD data, unless these additional phases increased the χ^2 values of the fitting procedure or yielded unphysical values of the refined parameters.

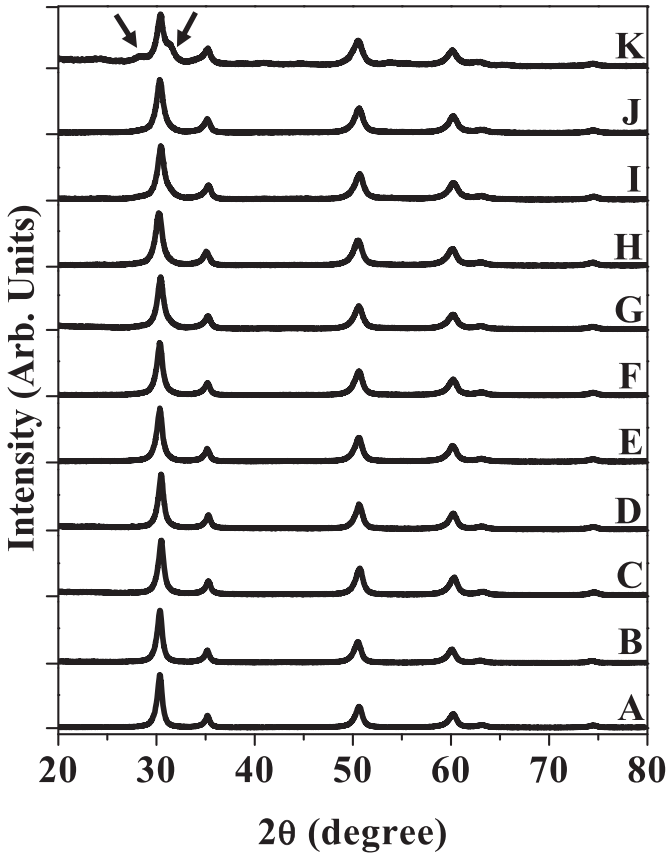

Fig. 1. XRD patterns of the as-prepared powder sample (Sample A) and the pellets made by compacting the sample at various pressures in the range 0.05–0.95 GPa (Sample B–Sample K). The additional features, which clearly appear in the pattern for the Sample K are shown by arrows in the topmost panel.

Fig. 3(a) plots the evolution of *T*-, *C*-, *M*- and *T′*- phase fractions with compacting pressure. The corresponding symbols for *C*-, *T*-, *M*- and *T′* - phase are squares (■), down triangles (▼), up triangles (▲), and circles (●), respectively. We find that new phases (*T′*- and *M*-) evolve in the system at the expense of the tetragonal phase, whereas the cubic phase fraction remains nearly unchanged. This is not surprising, as the high symmetry *C*-phase is more stable than a *T*-structure [18]. Fig. 3(b) plots the change is the lattice constants of *T*- and *C*- phases in the system with the increase in the compacting pressure. The open symbols show the lattice constant a_C of the *C*-phase, whereas, the filled symbols present the same (a_T and c_T) for the *T*-phase. It can be seen that under compacting pressure, the lattice parameter (a_C) of the *C*-phase remains nearly unchanged (○symbols in Fig. 3(b)). The lattice parameter c_T of the *T*-phase decreases beyond a certain compacting pressure (● symbols in Fig. 3(b)), while the value of a_T remains nearly constant (■ symbols in Fig. 3(b)).

It is noteworthy that the effect is observed on the green body, i.e., even without sintering the ceramic. In other words, the effect of temperature, which is commonly associated with such phase transitions, has no relevance in the present case; only the applied external pressure ascertains the observed phase transition. Secondly, the applied mechanical pressure is an order of magnitude smaller than the same reported in the literature for the phase transition in the related systems.

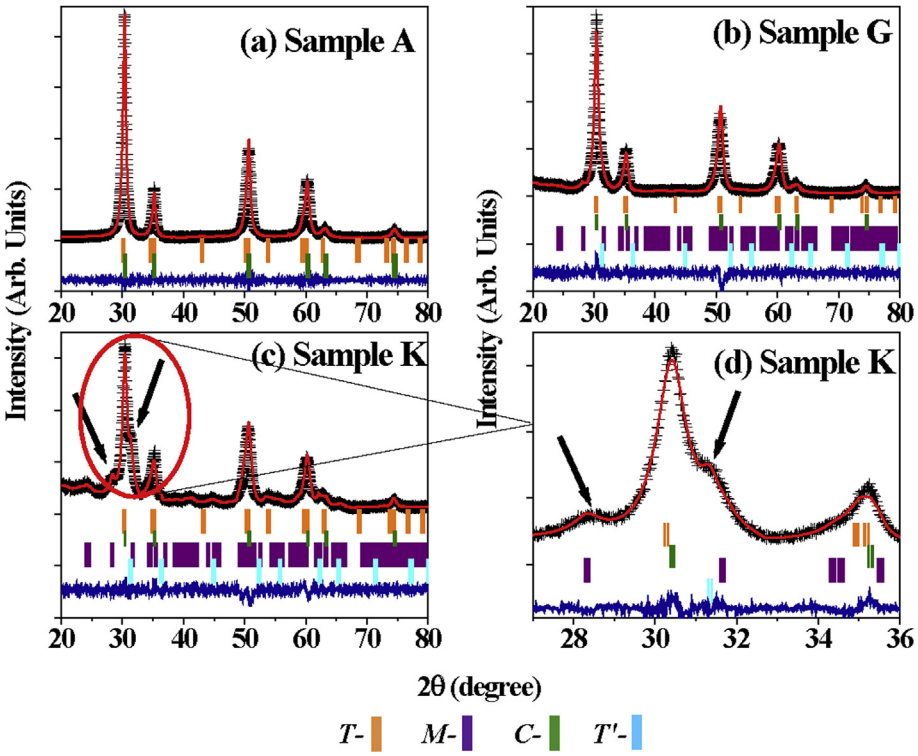

Fig. 2. Rietveld refined patterns of few selected samples, (a) powder (Sample A) and those pelletized at pressures (b) 0.55 GPa (Sample G), and (c) 0.95 GPa (Sample K). The enlarged view of the selected portion (within the red circle for Sample K in (c)) is shown in (d). The raw data points and net fitted patterns are shown with + symbols and the solid red lines, respectively. In each panel, the difference between the experimental and the calculated pattern is shown by the solid blue line. The Bragg reflection peaks corresponding to *C*-, *T*-, *M*- and distorted *T*'- phases are shown by green, orange, purple, and cyan bars, respectively. The additional features, which clearly appear in the pattern of the Sample K, are shown by arrows in panels (c) and (d). While the left arrow corresponds to the diffraction peak of the *M*-phase, the peak under the right arrow is contributed by both *M*- and *T*'- phases (see the text). (For interpretation of the references to colour in the figure legend, the reader is referred to the Web version of this article)

3.2. Raman scattering

To obtain further insight into the evolution of new phases in ZnO doped ZrO_2 under compacting pressure, as observed from XRD measurements, room temperature Raman spectra of the as-prepared powder sample (Sample A) and samples compacted under different mechanical pressures (Sample B to Sample K) were measured using 532 nm excitation wavelength and are shown in Fig. 4. For clarity, the whole spectral range is divided into two regions. We define the range from 125 cm^{-1} to 400 cm^{-1} as Region I and from 400 cm^{-1} to 750 cm^{-1} as Region II. In the spectral range between 125 and 750 cm^{-1}, several zone center (Γ) phonon modes of different phases of ZrO_2 contribute to the Raman spectra [9,10]. The frequencies of these vibrational modes of different phases of ZrO_2 are available in Table 2. Each spectrum in Fig. 4 is deconvoluted by considering a Lorentzian function for each expected mode and net Raman spectrum in each panel was fitted with $I(\omega) = \sum_{j=1}^{N} A_j \frac{\Gamma_j}{(\omega-\omega_j)^2+\Gamma_j^2}$, where A_j, Γ_j, ω_j are integral intensity, width, and Raman peak position for the jth observed mode, $I(\omega)$ is the net intensity, and N is the total number of modes. The Region-I and II are deconvoluted with eight ($N = 8$) and seven ($N = 7$) Lorentzian functions, respectively. In Fig. 4, solid orange lines are the deconvoluted components for the *T*-phase, and the solid purple lines are the same for the *M*-phase. The net fitted spectra are shown by the solid green lines. Since a large number of Raman peaks appear in the spectra and many of them nearly overlap, during the fitting procedure, we allowed the peak positions to vary only by 5% from the listed expected values in Table 2. Interestingly, though from XRD measurements the *M*-phase could be clearly detected only for the samples compacted at high pressure, the best fit of the Raman spectrum even of Sample A (as-prepared powder) could be obtained only after including the contribution of the Raman modes of the *M*-phase along with the modes of the *T*-phase and *C*-phase. This is not surprising as Raman spectroscopy is more sensitive than XRD measurements in detecting the *M*-phase of zirconia [28]. For example, for yttria-stabilized zirconia blocks, at a given composition, the *M*-fraction obtained by Raman spectroscopy is ~1.5–2 times higher than the same obtained from XRD measurements [29]. Referring to Table 2, we find that over the spectral range, shown in Fig. 4, the *C*- phase of ZrO_2 exhibits only one F_{2g} Raman mode at ~610 cm^{-1} [10]. It is also to be noted that very close to this Raman mode of the *C*-phase, A_{1g} mode of the *T*-phase and B_g mode of the *M*-phase appear at 613 cm^{-1} and ~615 cm^{-1}, respectively (refer to Table 2). Because of the large spectral width of the individual mode, these Raman peaks are expected to overlap in the recorded spectra. Thus, the deconvoluted component at 615 cm^{-1} (shown by the blue line) can be contributed either by *C*- or *M*- or *T*-phase or by all. Hence, from Raman spectral analysis, it is non-trivial to decipher the contribution of the *C*-phase, as revealed from the XRD measurements. Similarly, the Raman peak at 635 cm^{-1} of the *M*-phase is very close to the Raman mode of the *T*-phase at 640 cm^{-1} (refer to Table 2). Therefore, we refrain from assigning the Raman peak at 640 cm^{-1} (shown by the black line) to a specific phase. For a better visual clarity on the evolution of the *T*- and *M*-phases with the applied pressure, the deconvoluted components in the spectra for Sample A (bottom-most spectrum) and Sample K (just below the topmost spectrum) are shown by orange filled and purple filled regions for *T*- and *M*-phases, respectively. The mode, for which all three phases (*T*-, *M*-, and *C*-) may contribute, is shown by the cyan

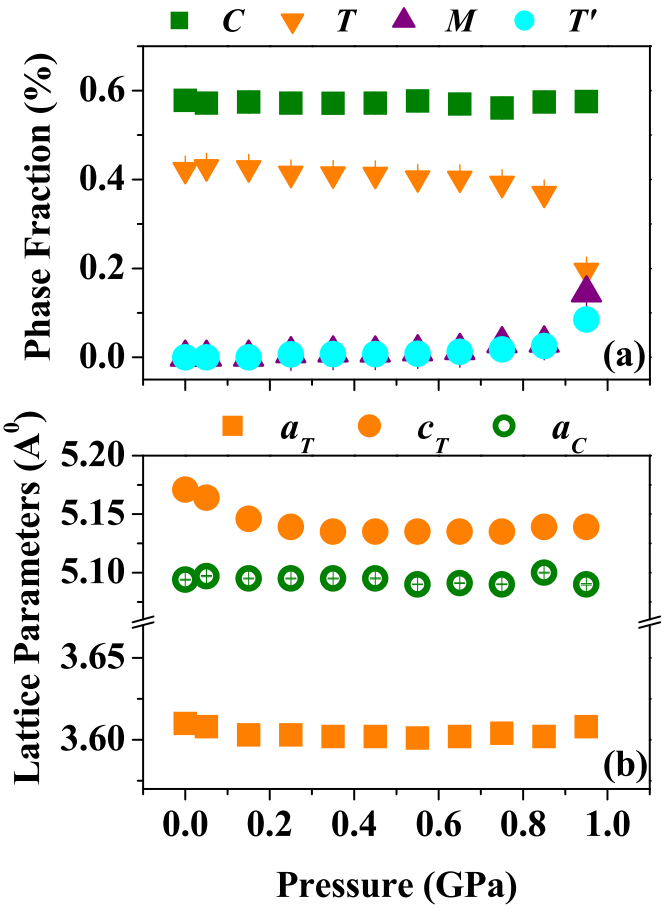

Fig. 3. (a) Evolution of *T*-, *C*-, *M*-, and *T*' - phase fractions with compacting pressure. The corresponding symbols for *C*-, *T*-, *M*-, and *T*' – phase are solid square (■), solid down triangle (▼), solid up triangle (▲) and solid circle (●), respectively. (b) The variation is the lattice constants of *T*- and *C*- phases in the system with compacting pressure. The lattice constant a_C for *C*-phase is given by open symbol (○), whereas, lattice constants a_T and c_T of the *T*-phase are given by solid symbols, ■and ●, respectively. The error bars to the data points (standard deviation of the fitted parameters) are nearly within the size of the symbols. (For interpretation of the references to colour in this figure legend, the reader is referred to the Web version of this article.)

filled area and the mode for which both *M*- and *T*-phases are expected to contribute is shown by the grey filled area. Here we would like to mention that the pressure-induced modified *T*-phase, i.e. *T*'- phase, as observed from XRD measurements in Fig. 2, is expected to give rise to new modes (which are Raman inactive for the *T*-phase) due to the breakdown of the selection rules or a change in the spectral line profile. The broad spectral line shapes restricted us to detect these changes in the net spectral profile. Thus, the presence of the *T*'- phase in the compacted samples could not be revealed from their Raman spectra.

Though some of the structural information, for example, the formation of *T*'-phase, *T*:*C* phase ratio, obtained from XRD measurements could not be revealed by the Raman data, we could exploit the later technique to find some other complementary information of the doped system, which could not be observed from the diffraction patterns. A careful look into the deconvoluted components in Fig. 4 indicates an increase in the *M*-phase with an increase in the mechanical pressure on the sample (i.e., from Sample B to Sample K). To study the *M*- and *T*-fraction in each sample and their evolution with the applied pressure, we have estimated the ratio of the integral intensity, as obtained from the curve fitting program, of each mode (I_i, $i = M$ or T for the modes related to *M*-phase or *T*-phase) with respect to the total intensity (I_{tot}) of all modes. The changes in these ratios for some prominent *M*- and *T*-modes with applied pressure are shown in Fig. 5. The error bar to each data point is estimated by using the standard deviation of the intensities, as a fitting parameter, and then using the propagation of error methodology. As the Raman modes are broad and overlapped, the fitting parameters are not unique. Hence, there is a large scattering of the data points in Fig. 5. Nonetheless, we observe a trend for the intensity ratio I_M/I_{tot} and I_T/I_{tot}. The *M*-phase fraction gradually increases with pressure (Fig. 5(a)–(f)) with a concurrent reduction in the *T*-phase fraction (Fig. 5(g)–(i)).

To investigate whether the *M*-phase has formed only near the surface or even in bulk, we have carried out wavelength dependent Raman measurements for the sample compacted at the highest pressure (Sample K (compacted at highest pressure 0.95 GPa)). The variation of both *T*-fraction [(I_{148}/I_{tot}), obtained for the *T*-mode at ~148 cm^{-1}] and *M*-fraction [(I_{175}/I_{tot}) for the *M*-mode at ~175 cm^{-1}] with excitation wavelengths are shown in Fig. 6(a) and (b), respectively. The error bars to the data points are obtained by following the same procedure as in Fig. 5. It is to be noted that the Raman peaks at 175 and 148 cm^{-1} are two distinct Raman features for the *M*- and *T*-phases in the sample respectively, and least contributed by the other Raman modes.

Wavelength dependent intensity of the Raman spectrum depends on various factors, like the penetration depth of the beam and the absorption coefficient of the material. It also varies inversely with the fourth power of laser wavelength. As we normalized the intensity of the above mentioned Raman modes with I_{tot}, we expect the ratio to remain constant for all wavelengths in case of the same phase fraction in the probing depth. We find in Fig. 6(a) that the intensity ratio I_{148}/I_{tot}, which indicates the *T*-phase fraction in the sample, increases beyond 647 nm as the excitation wavelength. However, for the ratio I_{175}/I_{tot}, which carries the

Table 1
The relative phase fraction (in percent) for ZnO doped ZrO_2 samples. The values in the bracket correspond to the estimated errors in the last two significant digits of the fitted values obtained from Rietveld refinement.

Sample	Applied pressure (GPa)	Tetragonal (*T*) phase	Cubic (*C*) phase	Monoclinic (*M*) phase	Distorted tetragonal (*T*') phase
A	0 (powder)	42.20(27)	57.80(31)	–	–
B	0.05	42.82(35)	57.18(50)	–	–
C	0.15	42.57(42)	57.43(66)	–	–
D	0.25	41.35(28)	57.19(57)	0.81(20)	0.65(12)
E	0.35	41.20(35)	57.14(68)	0.95(12)	0.71(12)
F	0.45	41.11(38)	57.19(72)	0.98(20)	0.73(12)
G	0.55	40.33(43)	57.65(25)	1.23(12)	0.80(18)
H	0.65	40.26(83)	56.98(88)	1.50(12)	1.25 (22)
I	0.75	39.07(82)	56.08(58)	3.07(22)	1.78(16)
J	0.85	36.83(25)	57.42(69)	3.20(38)	2.54(13)
K	0.95	19.50(25)	57.52(30)	14.47(40)	8.50(26)

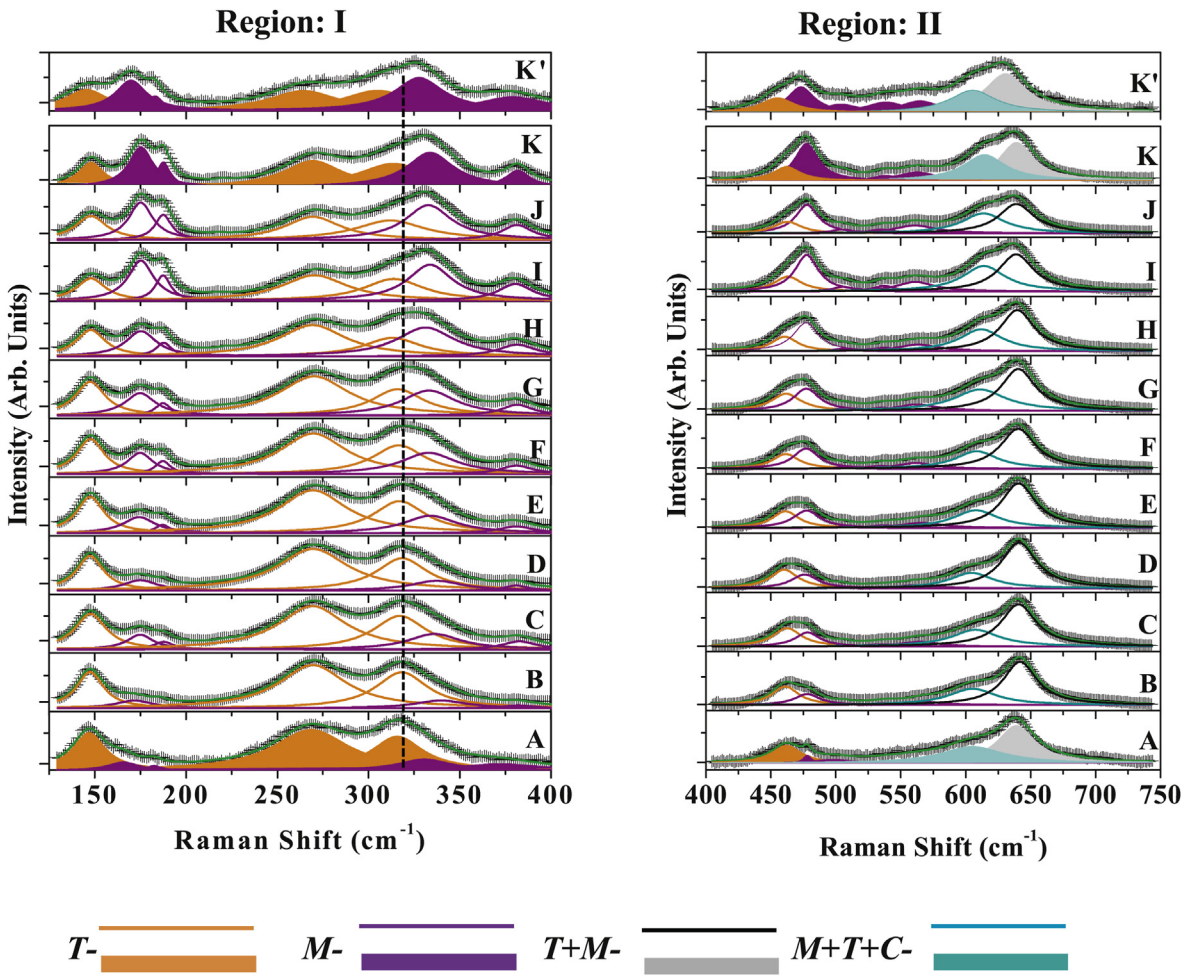

Fig. 4. Room temperature micro-Raman spectra of the powder sample (Sample A), calcined at 500 °C (A), and pellets made by compacting the sample at various pressures (Sample B−Sample K) in the range 0.05−0.95 GPa, recorded using 532 nm excitation wavelength. For each spectrum, raw data points are shown by (+) symbols, and the solid line (green) is the net fitted spectrum to the data points using Lorentzian function for all Raman modes. The Lorentzian modes for *T*- and *M*-phases are shown by orange and purple lines, respectively. The modes, which can be contributed by both *M*-, *T*- and *M*-, *T*-, *C*- phases are shown in black and blue solid lines, respectively (also see the marking in the bottom). The deconvoluted components for the *T*- and *M*-phases in the spectra for Sample A and Sample K are shown by orange filled and purple filled areas, respectively. In the spectra of these two samples, the modes for which both *T*- and *M*-phases can contribute and that for which all the three phases (*T*-, *M*- and *C*-) can contribute are shown by grey and cyan filled areas, respectively. The dashed line marks the shift in the B_{1g} mode of the *T*-phase, discussed in the text. The topmost spectra are for the Sample K′, see the text. (For interpretation of the references to colour in this figure legend, the reader is referred to the Web version of this article.)

signature of the *M*-phase fraction, we observe a significant drop in the intensity ratio beyond the above excitation wavelength (647 nm). The penetration depth of light of wavelength 632 nm in ZrO_2 is ~34 μm [30]. Though the number of data points above 650 nm is low due to unavailability of single-mode laser excitation wavelengths required for Raman measurements, Fig. 6 strongly indicates that the observed phase transformation (as revealed from XRD and Raman scattering measurements) dominates over this depth in the surface-subsurface regime of the compacted blocks.

The B_{1g} mode at ~322 cm^{-1} for the *T*-ZrO_2 (Refer to Table 2 and the dashed line in Fig. 4) involves sublattice expansion of zirconia [17]. Under harmonic approximation in an ionic crystal, polyhedral compressibility (κ) can be written as [17].

$$\kappa = 0.46\frac{\Delta\nu}{\nu}\frac{1}{\Delta P}.$$

Here, ν is the Raman shift of the B_{1g} mode, and Δν corresponds to the change in Raman shift due to the change in the pressure Δ*P*. In Fig. 7 we plot the variation in Raman shift of the B_{1g} mode (as obtained from the curve fitting) with the applied pressure (i.e., for

Table 2
Assignment of Raman modes of *M*-, *C*- and *T*-ZrO_2 [9,10].

Phase	Frequency (cm^{-1}) and Mode Assignment									
	Pure Modes					Mixed Modes				
	Colour code orange in Fig. 4		Colour code purple in Fig. 4			Colour code cyan in Fig. 4			Colour code grey in Fig. 4	
	B_{1g}	E_g	A_g+ B_g	A_g	B_g	F_{2g}	A_{1g}	B_g	E_g	A_g
Cubic	–	–	–	–	–	610	–	–	–	–
Tetragonal	148 322	261 464	–	–	–	–	613	–	640	–
Monoclinic	–	–	179 381	190 304 346 474 557	220 333 500 536	–	–	615	–	635

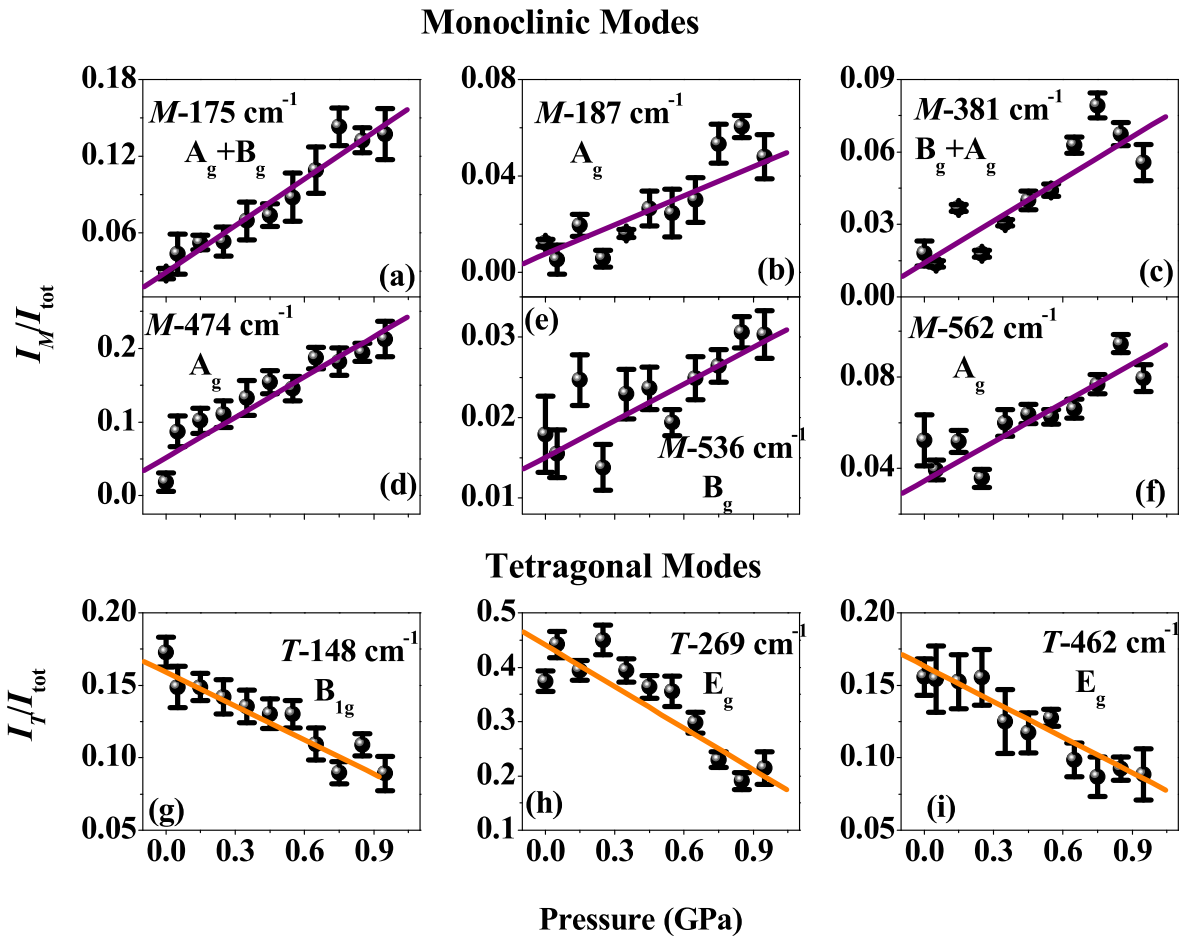

Fig. 5. The variation of (a)–(f) the *M*-fraction (I_M/I_{tot}) and (g)–(i) *T*-fraction (I_T/I_{tot}) (demonstrating the relative change in the amount of the phases) as a function of applied pressure. The error bar to each data point is calculated by using standard deviations of the intensities of the corresponding phases, as obtained from the curve fitting and following propagation of error methodology. The purple and the orange lines are guides to the eyes. (For interpretation of the references to colour in this figure legend, the reader is referred to the Web version of this article.)

Sample A-Sample K). The error bar to each data point is the standard deviation of the Raman shift as the fitting parameter in our curve fitting program. Though the observed Raman modes are broad, the shift in this mode with the increase in the compactness of the sample could be seen even by the naked eye (marked by the.dashed line Fig. 4). From Fig. 7, the value of the slope $\left(\frac{\Delta\nu}{\Delta P}\right)$ is estimated to be $5.9 \times 10^{-9}\text{cm}^{-1}\text{Pa}^{-1}$. The calculated value of the compressibility κ using the above expression is $\sim (8.6 \pm 1) \times 10^{-12}$ Pa^{-1}, which is comparable to the value 5×10^{-12} Pa^{-1} for undoped *T*-ZrO_2, as reported by Bouvier et al. [17]. To investigate the reversibility of the phase transition, we powdered the compacted pellet of the Sample K again and recorded its Raman spectrum. We name this sample as Sample K′. The spectral profile carried the signatures of the irreversible nature of the phase transformation process (see the panels in the top in Fig. 4 for Sample K′).

4. Discussion

The underlying mechanism for the observed compaction-induced phase transformation, as presented above, is expected to be different from what we find in most of the reports in the literature for Y_2O_3 and CaO doped systems under uniaxial or hydrostatic strain. Moreover, the compacting pressure applied on the pristine powder Sample A is an order of magnitude smaller than the same used to observe phase transition in the above mentioned doped compounds. To investigate the microscopic origin of the observed phase transformation in ZnO doped ZrO_2 under nominal pressure, we studied the energetically relaxed crystal structure of the supercell of ZnO doped ZrO_2 using DFT calculations. It is to be recalled that for the powder sample, *T*- and *C*- phases exist nearly in the ratio 1:1. From XRD and Raman scattering measurements (Figs. 3 and 5), we have observed an increase in the *M*-phase along with a decrease in the *T*-phase with the applied pressure. XRD patterns also revealed that the *C*-phase fraction remains nearly unchanged under compaction. Thus, to probe the effect of applied pressure on the crystal structure, we begin with the *T*-phase component in the crystal structure of ZnO doped ZrO_2 to construct the supercell in our DFT calculations.

For comparison, we first simulate the optimized structures of undoped ZrO_2 in the *M*- and *T*-phase. The lattice constants of the pure *M*-phase (space group $P2_1/c$) and *T*-phase (space group $P4_2/nmc$), are taken from Ref. [26]. Fig. 8(a) and (b) show the unit cell of the undoped *M*-phase and the *T*-phase of ZrO_2, respectively, as obtained from DFT calculations. The coordination numbers of Zr for *M*-ZrO_2 and *T*-ZrO_2 are seven and eight, respectively [31]. To study the doped system, we first construct the supercell of $2 \times 2 \times 2$ unit cells of the *T*- ZrO_2 (with space group $P4_2/nmc$) containing 48 atoms. For ZnO doped ZrO_2, one Zr^{+4} ion is replaced by one Zn^{+2} ion. As there are 16 Zr^{+4} ions in the supercell, on the replacement of a Zr^{+4} ion by a Zn^{+2} ion, we get 6.25% Zn doped ZrO_2. It is to be noted that this doping concentration of Zn is very close to the same

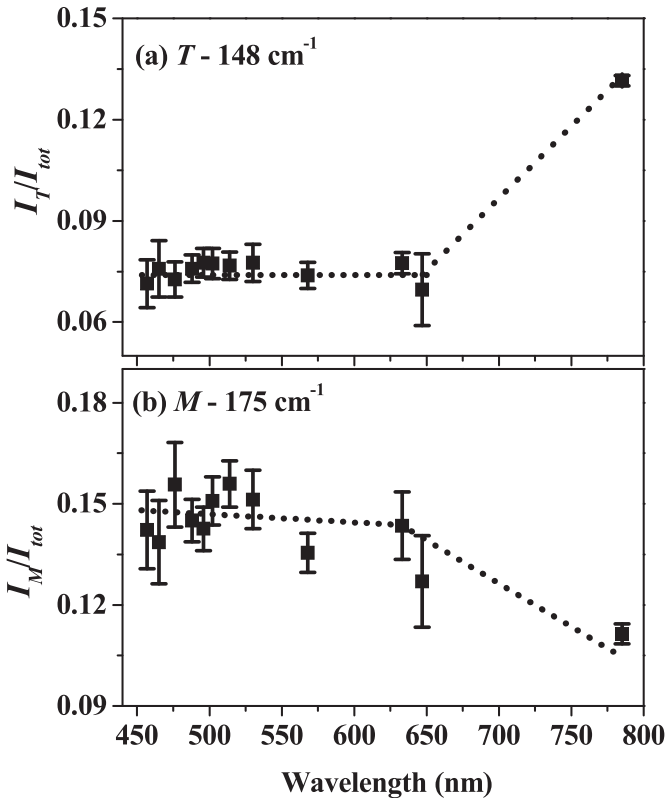

Fig. 6. The variation of the (a) *T*-fraction (I_T/I_{tot}) by considering the intensity of the Raman mode at 148 cm^{-1} and (b) *M*-fraction (I_M/I_{tot}) by considering the intensity of the Raman mode at 175 cm^{-1} as a function of incident wavelength for the Sample K (compacted at highest pressure 0.95 GPa). I_{tot} is the net intensity, including the same of all modes. The error bar to each data point is obtained by using standard deviations of the intensities, as obtained from the curve fitting and following the propagation of error methodology. The dotted lines are guides to eyes.

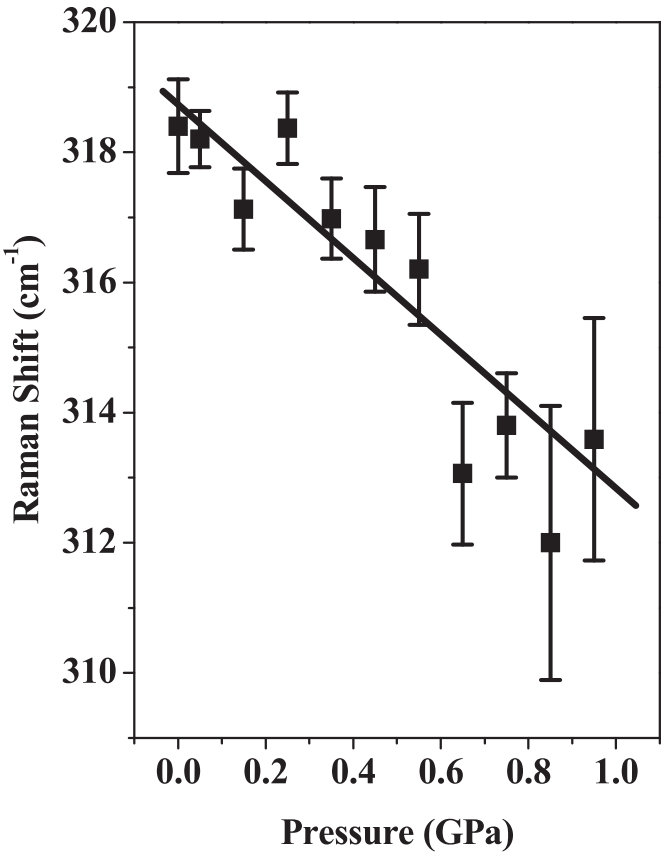

Fig. 7. The variation of the peak position of the B_{1g} mode (318 cm^{-1}) as a function of applied pressure (Sample A–Sample K). The error bar to each data point is the standard deviation of the Raman shift (as a parameter) in the fitting procedure. The solid line is a fit to the data points using linear regression.

that has been used experimentally (8%) and involves computationally inexpensive simulation. An O vacancy around the Zn atom maintains charge neutrality. To obtain the initial atomic positions in the supercell structure, we have used the experimental lattice constants of the *T*-phase as obtained from the Rietveld refinement of the XRD pattern of the Sample A (refer to Table 1). Fig. 8(c) presents the DFT-relaxed crystal structure of ZnO doped ZrO_2 of the *T*-phase. The doped Zn atom in the supercell is shown by a blue ball. The vacancy, introduced due to Zn^{2+} doping, is shown in the figure as a black ball and stick.

Table 3 lists Zr–O bond lengths in the unit cells of undoped *M*-ZrO_2 and *T*-ZrO_2. For undoped *M*-phase, there are seven different Zr–O bond lengths, whereas, for undoped *T*-ZrO_2, the crystal structure is relatively symmetric with two different sets of Zr–O bond lengths. The simulated optimized structure of Zn^{2+} doped ZrO_2 in Fig. 8(c) is expected to reveal the microscopic details of the crystal structure of the *T*-phase component of our doped system before compaction (mimic the powder Sample A). As the phase transformation involves changes in Zr–O bond lengths, to investigate the local environment of the doped compound, we have compared various Zr–O bond lengths in the undoped unit cell and doped supercell structures. A zoomed view of Fig. 8(c) is shown in Fig. 8(d). We find that in the supercell structure of the doped system, the nearest and the next nearest Zr atoms to Zn are in different environments, shown by the blue and the magenta polyhedra, respectively. We name these inequivalent Zr atoms as Zr1 (in blue polyhedron) and Zr2 (in magenta polyhedron). The various bond lengths involving Zr1 and Zr2 with O atoms are also available in Table 3. To investigate the pressure-induced structural changes, we studied the optimized structure of the supercell under the highest pressure of ~1 GPa, used in our experiments. The lattice constants of the supercell with and without applied pressure differed only by ~0.6% (see Fig. 3(b)). This change is too small to exhibit any structural phase transition. Zr1–O and Zr2–O bond lengths in the compressed supercell of the doped compound are estimated to be very similar to the listed values in Table 3 for the same in the uncompressed supercell. Furthermore, since the ionic radius of Zn^{2+} ion (~60 pm [5]) is much smaller than that of Zr^{4+} ion (84 pm), the Zn substitution is expected to render a negative pressure. Thus, it is unusual to observe *T*→*M* phase transition under compacting pressure as the calculated volumes of the unit cell of *M*-phase (138.9 $Å^3$) is much larger than that of *T*-ZrO_2 (66.9 $Å^3$).

The laws of thermodynamics govern pressure-induced structural phase transition. The lattice parameters are distinctly different in different phases. Structural disorder determines the entropy and enthalpy of the states in a complex way and allows or inhibits the phase transition. To understand the experimentally observed pressure-induced phase transition, as described in the previous section, we look into the structural environment, especially the bonding environment of Zr1 and Zr2 atoms in the supercell of the doped system shown in Fig. 8(c) and (d). We find that the Zr1 atom has coordination number 7 (same as Zr in undoped *M*-ZrO_2). Though the Zr1–O bond lengths are very different from those of undoped *M*- and *T*-phase ZrO_2, the average Zr1–O bond length (2.162 Å) is very close to the same of the undoped *M*-ZrO_2 (2.163 Å). Zr2 atom, next nearest to the doping site, has the coordination number 8 (same as Zr in undoped *T*-ZrO_2)

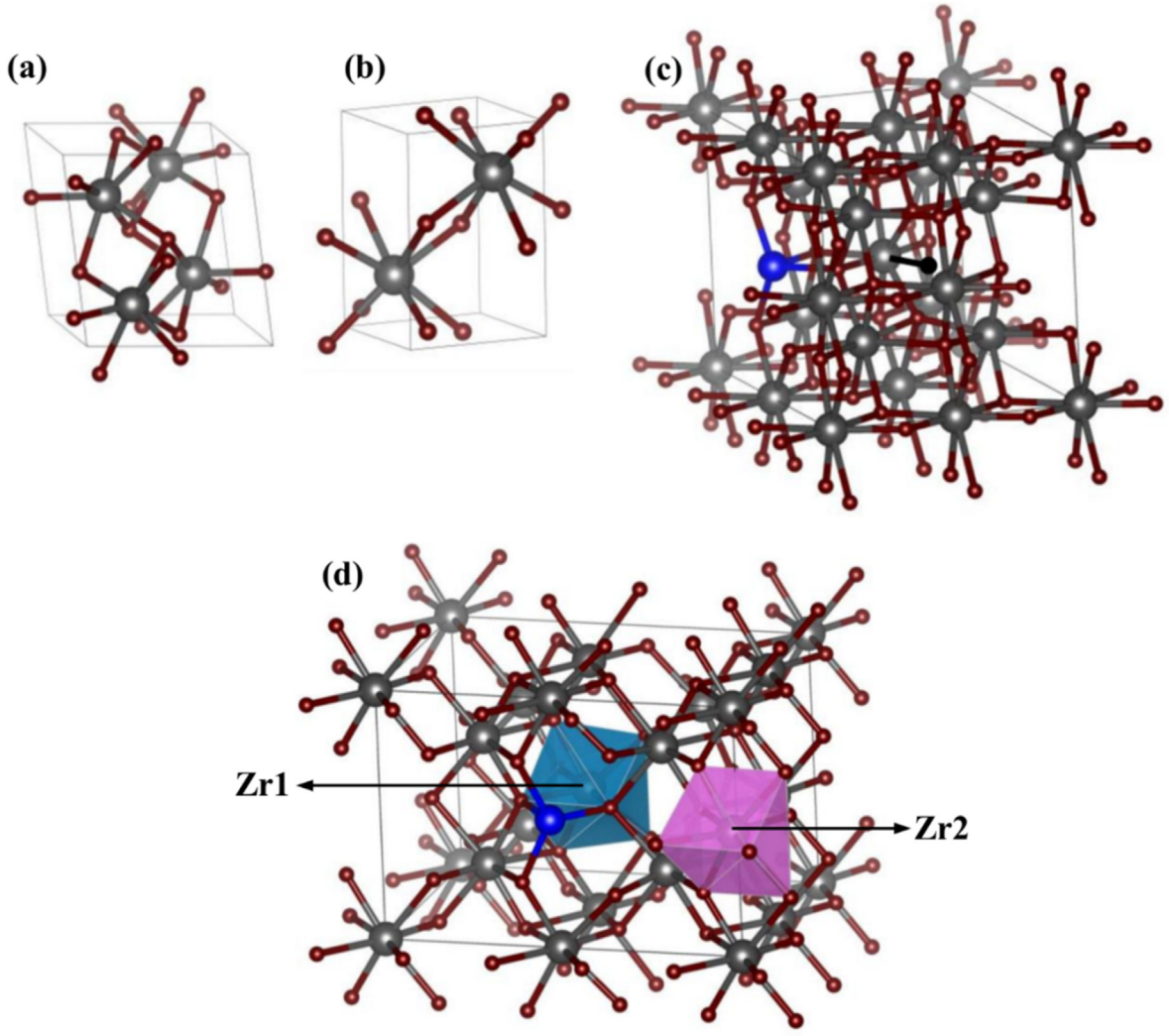

Fig. 8. Crystal structure of (a) undoped *M*-ZrO_2, (b) undoped *T*-ZrO_2, and (c) ZnO doped ZrO_2. The grey, red and blue balls represent Zr, O, and Zn atoms respectively. Impurity cation is surrounded by an O vacancy (black ball and stick). (d) Zoomed view of Fig. (c) to find the atomic distances near to the dopant (blue polyhedron) and far from the dopant (magenta polyhedron). The Zr atom in blue polyhedron is labeled as Zr1 and that in magenta polyhedron is labeled as Zr2, respectively. (For interpretation of the references to colour in this figure legend, the reader is referred to the Web version of this article.)

Table 3
Zr−O bond lengths of undoped *M*-, *T*-ZrO_2, and ZnO doped ZrO_2.

Zr−O bond distance in Å			
M-ZrO_2 Undoped	*T*-ZrO_2 Undoped	Zr1 (nearest to the doping site: in blue polyhedron)	Zr2 (next nearest to the doping site: in magenta polyhedron)
2.062	2.082	2.068	2.133
2.065	2.082	2.109	2.133
2.150	2.082	2.127	2.211
2.187	2.082	2.127	2.216
2.189	2.344	2.225	2.243
2.240	2.344	2.225	2.265
2.243	2.344	2.254	2.265
	2.344		2.319

and the individual bond lengths or the average bond length are very different from the values of the same in undoped *T*-phase, listed in Table 3. From above observations, we believe that the local structure around Zr1 atom is more susceptible to form the localized *M*-phase under an external perturbation (small pressure) in the real system at room temperature (DFT calculations are carried out for T = 0), while the Zr2 atom, next nearest to the doping site, gives rise to a low pressure-induced distorted *T*-phase(*T*′-phase). However, more detail calculations are needed to comment conclusively on it.

It is noteworthy that the muffin-tin radii of Zn and Zr are comparable, 1.95 and 2.0, respectively, in the constructed doped supercell. Thus, it is reasonable to believe that though the ionic radius of tetrahedrally coordinated Zn^{2+} is much smaller than that of Zr^{4+} (60 pm for Zn^{2+} in comparison to 84 pm for Zr^{4+}), the dopant can have a complex influence on the structural rearrangement of the host matrix.

As discussed earlier, a variety of pressure-induced structural responses are reported in the literature for doped zirconia. In all

these studies, although the phase transitions in the zirconia can be observed as the final effect, it remains customary to understand the mechanism by which the ZrO_2 matrix would accommodate the 'cause' factors (e.g., pressure, temperature, etc.) to induce or restrict a phase transition. We have shown the importance of the local structural environment, induced by doped metal cation, in understanding the phase integrity of the system. The appearance of the *M*-phase (by such low pressure) in ZrO_2 is detrimental for any engineering and medical applications [32]. The strength of zirconia declines sharply with an increase in the *M*-phase quotient. We believe that the understanding of phase transformation at a pressure (~1 GPa) has significant technological relevance as it matches with the pressure ranges for the shaping of the ceramics.

5. Conclusion

We have discussed the possible dynamics of structural phase evolution in ZnO-doped ZrO_2 under low scale (<1 GPa) compacting pressure, exploiting XRD, Raman scattering measurements, and DFT calculations. It is to be noted that the compacting pressure used in the present work is lower than the same reported in the literature for observing phase transition in doped and undoped ZrO_2. The Rietveld refinements of XRD patterns reveal the partial transformation of the *T*-host matrix to *M*-phase and distorted *T'*-phase. Raman spectral data confirm the evolution of the *M*-phase with the increase in the mechanical pressure and, in addition, indicate that the low symmetry phase forms only near-surface/subsurface region of the compacted block. The optimized supercell structure of the doped system, as obtained from the DFT calculations, reveals the importance of the local bonding environment around the dopant atom to explain the origin of the new phases, both *M*-and *T'*-, in a real system, under external perturbation.

Declaration of competing interest

The authors declare that they have no known competing financial interests or personal relationships that could have appeared to influence the work reported in this paper.

Acknowledgement

SM thanks DST for financial support under WOS-A scheme (Ref. No.: SR/WOS-A/PM-38/2017(G)). SM and AR thank Dr. A. Singha, Bose Institute of Basic Sciences, Kolkata, for Raman measurements using 632 nm and 785 nm laser wavelengths.

Appendix A. Supplementary data

Supplementary data related to this article can be found at https://doi.org/10.1016/j.jallcom.2020.155927.

References

[1] S. Starschich, U. Bottger, Doped ZrO_2 for future lead free piezoelectric devices, J. Appl. Phys. 123 (1–6) (2018), 044101.
[2] J. Chevalier, L. Gremillard, S. Deville, Low-temperature degradation of zirconia and implications for biomedical implants, Annu. Rev. Mater. Res. 37 (2007) 1–32.
[3] M. Pesic, S. Knebel, M. Geyer, S. Schmelzer, U. Böttger, N. Kolomiiets, V.V. Afanasev, K. Cho, C. Jung, J. Chang, H. Lim, T. Mikolajick, U. Schroeder, Low leakage ZrO_2 based capacitors for sub 20 nm dynamic random access memory technology nodes, J. Appl. Phys. 119 (1–5) (2016), 064101.
[4] S. Shibayama, T. Nishimura, S. Migita, A. Toriumi, Thermodynamic control of ferroelectric-phase formation in $Hf_xZr_{1-x}O_2$ and ZrO_2, J. Appl. Phys. 124 (1–7) (2018) 184101.
[5] R.D. Shannon, Revised effective ionic radii and systematic studies of interatomic distances in halides and chalcogenides, Acta Crystallogr. A 32 (1976) 751–767.
[6] C.W. Li, H.L. Smith, T. Lan, J.L. Niedziela, J.A. Munoz, J.B. Keith, L. Mauger, D.L. Abernathy, B. Fultz, Phonon anharmonicity of monoclinic zirconia and yttrium-stabilized zirconia, Phys. Rev. B 91 (1–8) (2015) 144302.
[7] M. Ohta, J.K. Wigmore, K. Nobugai, T. Miyasato, Influence of dopant ion on localized relaxation of an oxygen vacancy in stabilized zirconia, Phys. Rev. B 65 (1–8) (2002) 174108.
[8] A. Sobolev, A. Musin, G. Whyman, K. Borodianskiy, O. Krichevski, A. Kalashnikov, M. Zinigrad, Stabilization of cubic phase in scandium-doped zirconia nanocrystals synthesized with sol-gel method, J. Am. Ceram. Soc. 102 (2019) 3236–3243.
[9] B. Alzyab, C.H. Perry, R.P. Ingel, High-pressure phase transitions in zirconia and yttria-doped zirconia, J. Am. Ceram. Soc. 70 (1987) 760–765.
[10] J. Cai, Y.S. Raptis, E. Anastassakis, Stabilized cubic zirconia: a Raman study under uniaxial stress, Appl. Phys. Lett. 62 (1993) 2781–2783.
[11] J. Wang, G. Li, Z. Li, C. Tang, Z. Feng, H. An, H. Liu, T. Liu, C. Li, A highly selective and stable ZnO-ZrO_2 solid solution catalyst for CO_2 hydrogenation to methanol, Sci. Adv. 3 (1–10) (2017), e1701290.
[12] M.M. Ibrahim, Photocatalytic activity of nanostructured ZnO–ZrO_2 binary oxide using fluorometric method, Spectrochim. Acta Part A: Mol. Biomol. Spectrosc. 145 (2015) 487–492.
[13] E.D. Sherly, J.J. Vijaya, N.C.S. Selvam, L.J. Kennedy, Microwave assisted combustion synthesis of coupled ZnO–ZrO_2 nanoparticles and their role in the photocatalytic degradation of 2,4-dichlorophenol, Ceram. Int. 40 (2014) 5681–5691.
[14] A.O. de Souza, F.F. Ivashita, V. Biondo, A. Paesano Jr., D.H. Mosca, Structural and magnetic properties of iron doped ZrO_2, J. Alloys Compd. 680 (2016) 701–710.
[15] P. Bouvier, G. Lucazeau, Raman spectra and vibrational analysis of nanometric tetragonal zirconia under high pressure, J. Phys. Chem. Solid. 61 (2000) 569–578.
[16] W. Wang, Z. Liang, X. Han, J. Chen, C. Xue, H. Zhao, Mechanical and thermodynamic properties of ZrO_2 under high-pressure phase transition: a first-principles study, J. Alloys Compd. 622 (2015) 504–512.
[17] P. Bouvier, E. Djurado, G. Lucazeau, T. Le Bihan, High-pressure structural evolution of undoped tetragonal nanocrystalline zirconia, Phys. Rev. B 62 (2000) 8731–8737.
[18] V. Milman, A. Perlov, K. Refson, S.J. Clark, J. Gavartin, B. Winkler, Structural, electronic and vibrational properties of tetragonal zirconia under pressure: a density functional theory study, J. Phys. Condens. Matter 21 (1–12) (2009) 485404.
[19] C.H. Perry, F. Lu, D.W. Liu, B. Alzyab, Phonons and phase transitions in zirconia, J. Raman Spectrosc. 21 (1990) 577–584.
[20] H. Öztürk, M. Durandurdu, High-pressure phases of ZrO_2: an *ab initio* constant-pressure study, Phys. Rev. B 79 (1–6) (2009) 134111.
[21] D. Majumdar, D. Chatterjee, X-ray photoelectron spectroscopic studies on yttria, zirconia and yttria-stabilized zirconia, J. Appl. Phys. 70 (1991) 988–992.
[22] K. Kumar, T. Jaroń, A. Chowdhury, On the peculiarities of phase developments involving Zn^{2+}-doped ZrO_2 system, Scripta Mater. 138 (2017) 71–74.
[23] J. Rodriguez-Carvajal, Fullprof: A Program for Rietveld Refinement and Pattern Matching Analysis," Abstract of the Satellite Meeting on Powder Diffraction of the XV Congress of the IUCr, France, Toulouse, 1990, p. 127.
[24] P. Blaha, K. Schwarz, G. Madsen, , et al.K. Wien2, in: K. Schwarz (Ed.), An Augmented Plane Wave + Local Orbital Program for Calculating Crystal Properties, Technical University, Vienna, Austria, 2001.
[25] Z. Wu, R.E. Cohen, More accurate generalized gradient approximation for solids, Phys. Rev. B 73 (1–6) (2006) 235116.
[26] H. Tomaszewski, K. Godwod, Influence of oxygen partial pressure on the metastability of undoped zirconia dispersed in alumina matrix, J. Eur. Ceram. Soc. 15 (1995) 17–23.
[27] C.J. Howard, R.J. Hill, B.E. Reichert, Structures of ZrO_2 polymorphs at room temperature by high-resolution neutron powder diffraction, Acta Crystallogr. B44 (1988) 116–120.
[28] B. Kim, J. Hahn, K. Han, Quantitative phase analysis in tetragonal-rich tetragonal/monoclinic two phase zirconia by Raman spectroscopy, J. Mater. Sci. Lett. 16 (1997) 669–671.
[29] P.P. Kyaw, P. Pongprueksa, W. Anuchitolarn, K. Sirinukunwatta, K. Suputtamongkol, Ageing assessment of zirconia implant prostheses by three different quantitative assessment techniques, J Adv Prosthodont 11 (2019) 253–261.
[30] V. Presser, M. Keuper, C. Berthold, K.G. Nickel, Experimental determination of the Raman sampling depth in zirconia ceramics, Appl. Spectrosc. 63 (2009) 1288–1292.
[31] H. Ikeno, M. Krause, T. Hoche, C. Patzig, Y. Hu, A. Gawronski, I. Tanaka, C. Russel, Variation of Zr-$L_{2,3}$ XANES in tetravalent zirconium oxides, J. Phys. Condens. Matter 25 (1–8) (2013) 165505.
[32] A. Samran, A. Al-Ammari, S. El Bahra, E. Halboub, S. Wille, M. Kern, Bond strength durability of self-adhesive resin cements to zirconia ceramic: an in vitro study, J. Prosthet. Dent 121 (2019) 477–484.